

Hopf-chain networks

Jin Cai,¹ Yuee Xie,¹ Jinwoong Kim,² Po-Yao Chang,² Yuanping Chen^{1*}

¹*School of Physics and Optoelectronics, Xiangtan University, Xiangtan, Hunan, 411105, China*

²*Department of Physics and Astronomy, Rutgers University, Piscataway, New Jersey 08854-8019, USA*

Exotic links and chains attract interests across various disciplines including mathematics, biology, chemistry and physics. Here, we propose that topological Hopf-chain networks, consisting of one-, two- and three-dimensional (3D) Hopf chains, can be found in the momentum space. These networks can be evolved from a 3D triple-points phase by varying symmetries of a four-band model. Moreover, we identify that the Hopf-chain networks exist in a family of crystals Sc_3XC ($X = \text{Al, Ga, In, Tl}$). The crystals are 3D triple-points metals, and transit to topological metals with Hopf-chain networks under strains. These novel Hopf networks exhibit unique Landau levels and magneto-transport properties.

* Corresponding email: chenyp@xtu.edu.cn

Hopf link, consisting of two rings linked together exactly once (see Fig. 1(a)), is the simplest nontrivial link with more than one component, according to mathematical knot theory^{1,2}. Hopf links can be further periodically linked to a one-dimensional (1D) Hopf chain in Fig. 1(b), whose unit length is labeled as the light-blue dashed line³. A complicated 1D Hopf chain with a unit of two linked Hopf links is shown in Fig. 1(c).

Hopf links and chains have captured attentions of not only mathematicians but also biologists, chemists and physicists⁴⁻¹². In biology, Hopf links have been found in DNA and synthesized in template synthesis, which are believed to be functionally advantageous and provide extra stability to protein chains⁴⁻⁶. In chemistry, Hopf links are well known in catenanes, a kind of compounds that consist of molecular rings held together by mechanical bonds⁷⁻⁹.

In physics, the studies of topological semimetals/metals (TMs) indicated that Fermi surfaces, crossed by conduction and valence bands in the momentum space, can exhibit diverse patterns¹³⁻³⁸, such as points, lines and surfaces. Weyl, Dirac and triple points are representatives of topological nodal points¹³⁻²⁰. Comparing with nodal points, nodal lines are more flexible to form diverse topologically distinct objects²¹⁻³⁴, such as rings²¹⁻²⁵, knots^{26, 27} and nets^{28, 29}. A Hopf link, as a kind of typical topological phase including two rings³⁰⁻³⁴, has been proposed and obtained in Co_2MnGa ³⁰. It shows unique topological characteristics and transport properties different from isolated and intersecting rings. A simple Hopf chain shown in Fig. 1(b) has also been found in a 3D pentagon carbon³². This topological phase is generated by three energy band crossings, which not only reveals novel Hopf-link fermions but also exhibits special Landau levels.

Mathematically, 1D Hopf chains can be used to construct two-dimensional (2D) and three-dimensional (3D) networks, named as Hopf-chain networks, by linkages

between chains. Figures 1(d-e) present two 2D networks consisting of two mutually vertical chains along X and Y axes, where the intersections of the chains locate at the ordinate origin. The light-blue dashed boxes show units of the networks. The difference between the two networks is that the two vertical chains in Fig. 1(e) share a blue ring while those in Fig. 1(d) intersect each other. Figure 1(f) presents a 3D network, which consists of a 2D network like that in Fig. 1(e) and a 1D simple chain along Z direction. Moreover, the 1D chain crosses over the 2D network without any contacts. Obviously, more 2D and 3D Hopf-chain networks can be obtained by different linkages between Hopf links and chains. We use a parameter D_l^r to label different chains and networks, where D represents dimensions, r represents the number of rings in a unit, while l is linking number between rings in the unit³⁴. In this case, the parameters for Figs. 1(b-f) are 1_1^2 , 1_3^4 , 2_2^4 , 2_2^3 and 3_3^5 , respectively. To date, the 2D and 3D Hopf-chain networks have not been found in momentum space.

Here, we propose that the Hopf-chain networks can be evolved from spinless triple-points systems with multiple four-fold (C_4) rotation and mirror symmetries (all triple points in this work refer to spinless triple points unless otherwise specified). For example, when a system has three mutually vertical C_4 rotation axes and three mutually vertical mirrors, a topological phase including 7 triple points can be obtained, as shown in Fig. 3(a), based on a four-band $\mathbf{k} \cdot \mathbf{p}$ model. It evolves into a series of 3D topological networks when the structural symmetry is reduced. The evolved networks include the Hopf-chain networks in Fig. 1, as shown in Figs. 3(b-d). Moreover, we identify that these networks can be observed in the crystals Sc_3XC ($X = \text{Al, Ga, In, Tl}$) under uniaxial or biaxial strains. The symmetry requirements for the appearance of different networks are analyzed. In addition, Landau levels and topological surface states of the networks are discussed.

Results

1D Hopf chain evolved from triple points

We start from a simplest Hopf chain evolved from triple points in the momentum space³². In a system with a 4-fold rotation axis (along k_z) and two mirror planes ($k_x = 0$ and $k_y = 0$), a triple-points phase based on a three bands model can be obtained, which is shown in Fig. 2(a) and its corresponding band structures are shown in Figs. 2(b-c). The phase is generated by three bands. Two of the bands are degenerate along k_z , as shown in Fig. 2(b), and they cross linearly with another band, which results in two triple points T. The degenerate band is in fact a nodal line. Each point on the nodal line is a crossing point of two quadratic bands along k_x (or k_y), as shown in Fig. 2(c), and thus the Berry phase around the point is 2π . Therefore, the two triple points are linked by a red nodal line (see Fig. 2(a)). When the C_4 rotation symmetry is eliminated but the two mirror planes are held on, the triple points evolve into a 1D Hopf chain in Fig. 2(d), i.e., Fig. 1(b). Figures 2(e-f) present band structures for the Hopf chain. The reduced symmetry leads to the lift of the degenerate band, meanwhile the triple points T split to two crossing points W_1 and W_2 . The two points W_1 and W_2 locate on two vertical rings of the Hopf chain, respectively. The two rings are protected by the mirror planes $k_x = 0$ and $k_y = 0$. Two cases for the Hopf chain exist: one is the central ring on the plane $k_x = 0$ like that in Fig. 3(b), the other is the central ring on the plane $k_y = 0$. The two cases are related to the mirror eigenvalues of the two splitting bands. When the mirror eigenvalues of the two bands for point W_1 are $(X+, Y-)$ and $(X-, Y-)$ ($X\pm$ and $Y\pm$ represent the eigenvalues of mirror operators on the planes $k_x = 0$, $k_y = 0$ being ± 1), the central nodal ring locates on the plane $k_x = 0$ because the two mirror eigenstates are orthogonal to each other on the mirror plane. Otherwise, the central nodal ring locates on the plane $k_y = 0$ when the mirror eigenvalues are $(X-, Y+)$ and $(X-, Y-)$. The nodal

rings in the Hopf chain have a nontrivial Berry phase π .

2D and 3D Hopf-chain networks based on a $\mathbf{k} \cdot \mathbf{p}$ model

To obtain 2D and 3D Hopf-chain networks, a four-band $\mathbf{k} \cdot \mathbf{p}$ model with three normal 4-fold rotation axes along k_x, k_y, k_z and three mirror planes on $k_x = 0, k_y = 0, k_z = 0$ is required. Considering the symmetry, the system should also have three equivalent orbitals along x, y and z , respectively. In this sense, p_x, p_y, p_z and d_{xy}, d_{yz}, d_{zx} can be candidates. Here, we use three d orbital bands and one s orbital band to construct a $\mathbf{k} \cdot \mathbf{p}$ model written as³⁹

$$H(\mathbf{k}) = \begin{bmatrix} f_1 & Ak_x k_y & Bk_x k_z & Ck_y k_z \\ Ak_x k_y & f_2 & Dk_y k_z & Ek_x k_z \\ Bk_x k_z & Dk_y k_z & f_3 & Fk_x k_y \\ Ck_y k_z & Ek_x k_z & Fk_x k_y & f_4 \end{bmatrix}, \quad (1)$$

where $f_i = a_i + b_i k_x^2 + c_i k_y^2 + d_i k_z^2$. Because of the three normal 4-fold rotational symmetry, the parameters should satisfy $a_1 = a_2 = a_3, b_1 = c_2 = d_3, b_2 = b_3 = c_1 = c_3 = d_1 = d_2, b_4 = c_4 = d_4, A = B = D, C = E = F$.

By tuning the parameters, we obtain a phase including 7 triple points, as shown in Fig. 3(a). There are a pair of triple points on each axis, and there is another triple point at the center Γ of BZ. The band structures along three axes are given in Fig. 3(e). Beside the top parabolic band, the band structures are similar to that in Fig. 2(b): a degenerate band crosses linearly with the other single band, which generates six triple points T_1 on $k_x/y/z$ axis, and these triple points are linked by straight nodal lines along axes. The top parabolic band in Fig. 3(e) introduces additional triple point T_2 at Γ point which quadratically touches the degenerate band. Therefore, the phase in Fig. 3(a) is a 3D

version of the 1D triple points phase in Fig. 2(a) adding an extra triple point at Γ point, i.e., a 3D triple-points phase.

When one C_4 rotation symmetry, for example, the C_4 symmetry along k_y , is broken, another C_4 rotation symmetry will also be broken, say k_x . Then, only the C_4 rotation symmetry along k_z is held on. Different values of the parameters will result in two different topological phases, as shown in Figs. 3(b) and 3(c), respectively. The band structure corresponding to the phase in Fig. 3(b) is shown in Fig. 3(f). The degenerate band along k_x and k_y axes is lifted by the broken C_4 rotation symmetries, and the triple point T_1 on $k_{x/y}$ axis splits to two crossing points. This induces the transition on k_x and k_y axes from triple points to Hopf chain like that from Fig. 2(a) to 2(d). Seen from the mirror eigenvalues of the crossing bands, the central rings of the mutually orthogonal chains locate on the planes $k_x = 0$ and $k_y = 0$, respectively, and they contact each other on the k_z axis forming intersecting rings. As a result, the 2D Hopf-chain network discussed in Fig. 1(d) is materialized as shown in Fig. 3(b). Along k_z axis, the two triple points still exist because of the C_4 rotation symmetry is reserved. If we consider the top band, the lift of the degenerate band leads to disappearance of the triple point T_2 at Γ point. The triple point T_2 evolves into a nodal ring with center at Γ point on the plane $k_z = 0$. The whole topological phase is shown in Fig. 3(b), which is a mixture of a 2D Hopf-chain network, a nodal ring and two triple points.

Another phase resulted from breaking two C_4 rotation symmetries is shown in Fig. 3(c), and its corresponding band structure is given in Fig. 3(g). By comparing Figs. 3(f) and 3(g), one can find that the brown band shifts down in Fig. 3(g). The shifting exchanges the mirror eigenvalues of bands, which results in the central nodal rings of the two chains both locate on the plane $k_z = 0$ instead of the two vertical mirror planes.

The two rings combine together to a distorted ring which is shared by the two Hopf chains. Obviously, the two orthogonal chains form a 2D Hopf-chain network similar to that in Fig. 1(e). Another change induced by the shifting band is the original triple point at Γ point in Fig. 3(a) transits to two triple points along k_z axis. Therefore, the topological phase in Fig. 3(c) shows a mixture of a 2D Hopf-chain network and four triple points on k_z axis.

Next, we consider the case that all the three C_4 rotation symmetries are broken while the three mirror planes are still held on. In this case, the constraints to all parameters in Eq. (1) are released. Figure 3(d) shows a topological phase evolved from Fig. 3(c) (or Fig. 3(b)), and the corresponding band structure is given in Fig. 3(h). Because all the C_4 rotation symmetries are eliminated, the degenerate bands along all axes split, and thus the two couples of triple points on k_z axis in Fig. 3(C) split to a complicated 1D Hopf chain along k_z axis. The emergent Hopf chain along k_z axis is similar to that in Fig. 1(c). This Hopf chain and the 2D Hopf chain along k_x and k_y axes form a 3D Hopf-chain network. [The detailed values of the parameters for all phases are shown in Table S1 in supplementary information (SI)] It is noted that, additional topological networks can be obtained by tuning the parameters in Eq. (1) [see Fig. S1].

Hopf-chain networks realized in real crystals

In order to realize these topological phases in real crystals, the crystal structures should have three C_4 rotation symmetries along x, y and z axes and mirror planes on the three coordinate planes. We find that the family of Sc_3XC ($X = \text{Al, Ga, In, Tl}$), which crystallizes in cubic structure with space group PM-3M(OH-1) , can meet the requirement. Their atomic structures are schematically shown in Fig. 4(a). The element C is located at the center and the atoms Sc and X are located at the face center and the

cubic corner, respectively. Their structural parameters are shown in Table S2 in SI. The electronic, mechanical, and optical properties of these materials have been studied^{40, 41}. However, their topological properties have not been discussed yet.

We calculate the band structures of these crystals, by using the first principles. All the crystals have very similar band structures (see Fig. S2 in SI). Figure 4(c) show the band spectrum of Sc_3InC in the case of no spin-orbit coupling (SOC). When SOC is absent, the system can be considered as a spinless system. One can find that the band spectrum along Γ -X is very similar to that in Fig. 2(a): there is a triple point on k_x axis and a triple point at the Γ point. Therefore, these structures possess the 3D triple-points phase in Fig. 3(a). By applying different strains, the topological phase evolves into various other phases which have been obtained by the $\mathbf{k} \cdot \mathbf{p}$ model. For example, when a hydrostatic pressure is applied on the crystals, the phase is changed from Fig. 3(a) to Fig. S2(a), i.e., a distorted rectangular ring is added to each mirror plane of the phase. When a tensile or a compressive strain is applied on z axis to eliminate the two C_4 rotation symmetries along x and y axes, mixture phases in Figs. 3(b-c) can be obtained, respectively. When a strain is further applied on x or y axis to eliminate the final C_4 rotation symmetry, the phase evolves to a 3D Hopf-chain network like that in Fig. 3(d). Band structures corresponding to the phases as well as contour plots for energy differences of bands are given in Fig. S3.

If SOC is considered, the original triple points and nodal rings are gapped (see Fig. S4 and insets in Fig. 4(c)). Each band is still doubly degenerate because of the presence of inversion symmetry. Because the gaps of nodal rings are very small (only $1 \sim 6$ meV), as shown in Fig. S4, the Hopf-chain networks discussed above can be observed experimentally.

Surface states and Landau levels of Hopf-chain networks

The Hopf chain consists of mutually orthogonal rings. The rings can be projected on the mutually vertical surfaces and lead to drumhead states respectively. The calculations of surface states for Sc_3InC identify existence of the drumhead states, as shown in Fig. S5. On the surfaces of the 3D triple-points phase, there are “tent” states between the triple points [see Figs. S5(a₁-a₃)]. These surface states evolve into drumhead states after the triple points evolve into Hopf chains. For example, for the 2D Hopf-chain phases in Figs. 3(b) and 3(c), the nodal rings are projected on the surfaces [100] and [001], respectively, and thus drumhead states are found on the two surfaces [see Figs. S5(b₁-c₃)]; moreover, the distributions of the nodal rings in the two phases are inverse, which results in inverse surface states, i.e., the surface state on the surface [100] for the phase in Fig. 3(b) corresponds to that on the surface [001] for the phase in Fig. 3(c).

We also calculate the Landau levels of the four phases in Figs. 3(a-d) based on the $\mathbf{k} \cdot \mathbf{p}$ model, as shown in Fig. S6. One can find that there are two kinds of Landau levels in the spectra. One is chiral modes induced by the triple points, the other is zeroth modes induced by the nodal rings. In the topological phases in Fig. 3(a-c), there are triple points along k_z axis, and thus chiral modes appear on the spectra in Fig. S6(a-c). Especially in the phase of Fig. 3(c), there are two pairs of triples points, correspondingly, one can find two sets of chiral modes between them. After all the triple points split to nodal rings, in Fig. S6(d), zeroth modes inner the projection of nodal rings can be observed.

Discussion

In real materials, the triple points and the Hopf-chain networks are not exactly located at the Fermi level. Therefore, many electron and hole pockets exist near the Fermi level, which results in semimetallic behavior in terms of transports. Under the low magnetic field, these materials are expected to have extreme magnetoresistance due to the compensation between the electron and hole carriers⁴²⁻⁴⁴. In the quantum region, when the quantized Landau orbits lead to quantum oscillations, one can expect the magnetic breakdown due to the tunneling between electron and hole pockets. The magnetic breakdown are strongly dependent on the direction of the magnetic field⁴⁵. In the case of Hopf-chain network extending on the k_x - k_y plane (see Fig. 1(e)), one can expect strong magnetic breakdown when the field is along the k_z direction. On the other hand, in the case of Hopf-chain network extending on the entire Brillouin zone (see Fig. 1(f)), profound magnetic breakdown can be observed in all three axes.

The Hopf-chain networks discussed here are related to a four-band case. One can expect that more abundant Hopf-chain networks can be found in multi-band cases. These exotic Hopf patterns are common interests of mathematics, biology, chemistry and physics. Therefore, our work not only provides new topological phases and emergent fermions in physics, but also opens a door for other fields to explore the beautiful motifs.

Methods

Computational methods. We performed first-principles calculations within the density functional theory (DFT) as implemented in the VASP codes^{46, 47}. The potential of the core electrons and the exchange-correlation interaction between the valence electrons were described, respectively, by the projector augmented wave⁴⁸ and the generalized gradient approximation (GGA) with Perdew-Burke-Ernzerhof (PBE)⁴⁹

functional. A kinetic energy cutoff of 550 eV was used. The atomic positions were optimized using the conjugate gradient method, and the energy and force convergence criteria were set to be 10^{-5} eV and 10^{-3} eV/Å, respectively. The Brillouin zone (BZ) was sampled in the k space within the Monkhorst-Pack scheme and the number of these k points was $7 \times 7 \times 7$. The surface energy dispersions were calculated within the tight binding scheme based on the maximally localized Wannier functions (MLWFs), using the Wannier-tools software package⁵⁰.

Acknowledgments

We thank the discussions with Heung-Sik Kim. This work was supported by the National Science Foundation of China (No. 11474243 and No. 51376005).

Author contributions

Y.C. conceived the original ideas. All authors discussed the results and commented on the manuscript at all stages.

Additional information

Supplementary Information accompanies this paper at <http://www.nature.com/nature communications>

Competing interests: The authors declare no competing financial interests.

References

1. Adams CC, Govindarajan T. The Knot Book: An Elementary Introduction to the Mathematical Theory of Knots. *Phys Today* **48**, 89 (1995).
2. Birman JS. New points of view in knot theory. *Bull Amer Math Soc* **28**, 253-287 (1993).
3. Proserpio DM. Topological crystal chemistry: Polycatenation weaves a 3D web. *Nat Chem* **2**, 435 (2010).
4. Liang C, Mislow K. Knots in proteins. *J Am Chem Soc* **116**, 11189-11190 (1994).
5. Chen J, Rauch CA, White JH, Englund PT, Cozzarelli NR. The topology of the kinetoplast DNA network. *Cell* **80**, 61-69 (1995).
6. Dabrowski-Tumanski P, Sulkowska JI. Topological knots and links in proteins. *Proc Natl Acad Sci*, **114**, 3415-3420 (2017).
7. Jin C-M, Lu H, Wu L-Y, Huang J. A new infinite inorganic [n] catenane from silver and bis (2-methylimidazolyl) methane ligand. *Chem Commun*, 5039-5041 (2006).
8. Westcott A, Fisher J, Harding LP, Rizkallah P, Hardie MJ. Self-assembly of a 3-D triply interlocked chiral [2] catenane. *J Am Chem Soc* **130**, 2950-2951 (2008).
9. Fang L, Olson MA, Benitez D, Tkatchouk E, Goddard WA, 3rd, Stoddart JF. Mechanically bonded macromolecules. *Chem Soc Rev* **39**, 17-29 (2010).
10. Jampani VSR, Škarabot M, Ravnik M, Čopar S, Žumer S, Mušević I. Colloidal entanglement in highly twisted chiral nematic colloids: Twisted loops, Hopf links, and trefoil knots. *Phys Rev E* **84**, 031703 (2011).
11. Romero J, *et al.* Entangled optical vortex links. *Phys Rev Lett* **106**, 100407 (2011).
12. Li L, Chesi S, Yin C, Chen S. 2π -flux loop semimetals. *Phys Rev B* **96**, (2017).
13. Hasan MZ, Xu S-Y, Belopolski I, Huang S-M. Discovery of Weyl fermion semimetals and topological Fermi arc states. *Annual Review of Condensed Matter Physics* **8**, 289-309 (2017).
14. Sun Y, Wu S-C, Ali MN, Felser C, Yan B. Prediction of Weyl semimetal in orthorhombic MoTe₂. *Phys Rev B* **92**, 161107 (2015).
15. Liu CC, Zhou JJ, Yao Y, Zhang F. Weak Topological Insulators and Composite Weyl Semimetals: beta-Bi₄X₄ (X=Br, I). *Phys Rev Lett* **116**, 066801 (2016).
16. Armitage N, Mele E, Vishwanath A. Weyl and Dirac semimetals in three-dimensional solids. *Rev Mod Phys* **90**, 015001 (2018).
17. Liu Z, *et al.* Discovery of a three-dimensional topological Dirac semimetal, Na₃Bi. *Science* **343**, 864-867 (2014).

18. Liu Z, *et al.* A stable three-dimensional topological Dirac semimetal Cd_3As_2 . *Nat Mater* **13**, 677 (2014).
19. Weng H, Fang C, Fang Z, Dai X. Topological semimetals with triply degenerate nodal points in θ -phase tantalum nitride. *Phys Rev B* **93**, 241202 (2016).
20. Ma J-Z, *et al.* Three-component fermions with surface Fermi arcs in tungsten carbide. *Nature Physics*, **14**, 349-354 (2018).
21. Huang H, Liu J, Vanderbilt D, Duan W. Topological nodal-line semimetals in alkaline-earth stannides, germanides, and silicides. *Phys Rev B* **93**, 201114 (2016).
22. Pang G, *et al.* Nodeless superconductivity in noncentrosymmetric PbTaSe_2 single crystals. *Phys Rev B* **93**, 060506 (2016).
23. Gao Y, Chen Y, Xie Y, Chang P-Y, Cohen ML, Zhang S. A class of topological nodal rings and its realization in carbon networks. *Phys Rev B* **97**, 121108 (2018).
24. Gong C, Xie Y, Chen Y, Kim HS, Vanderbilt D. Symmorphic Intersecting Nodal Rings in Semiconducting Layers. *Phys Rev Lett* **120**, 106403 (2018).
25. Bian G, *et al.* Topological nodal-line fermions in spin-orbit metal PbTaSe_2 . *Nat Commun* **7**, 10556 (2016).
26. Bi R, Yan Z, Lu L, Wang Z. Nodal-knot semimetals. *Phys Rev B* **96**, 201305 (2017).
27. Dennis MR, King RP, Jack B, O'Holleran K, Padgett MJ. Isolated optical vortex knots. *Nat Phys* **6**, 118 (2010).
28. Wang J-T, Nie S, Weng H, Kawazoe Y, Chen C. Topological Nodal-Net Semimetal in a Graphene Network Structure. *Phys Rev Lett* **120**, 026402 (2018).
29. Feng X, Yue C, Song Z, Wu Q, Wen B. Topological Dirac nodal-net fermions in AlB_2 -type TiB_2 and ZrB_2 . *Physical Review Materials* **2**, 014202 (2018).
30. Chang G, *et al.* Topological Hopf and Chain Link Semimetal States and Their Application to Co_2MnGa . *Phys Rev Lett* **119**, 156401 (2017).
31. Zhou Y, Xiong F, Wan X, An J. Hopf-link topological nodal-loop semimetals. *Phys Rev B* **97**, 155140 (2018).
32. Zhong C, *et al.* Three-dimensional Pentagon Carbon with a genesis of emergent fermions. *Nat Commun* **8**, 15641 (2017).
33. Chen W, Lu H-Z, Hou J-M. Topological semimetals with a double-helix nodal link. *Phys Rev B* **96**, 041102 (2017).
34. Baas NA. New states of matter suggested by new topological structures. *Int J Gen Syst* **42**, 137-169 (2013).
35. Wu W, *et al.* Nodal surface semimetals: Theory and material realization. *Phys Rev B* **97**, 115125 (2018).

36. Türker O, Moroz S. Weyl nodal surfaces. *Phys Rev B* **97**, 075120 (2018).
37. Zhao J, Yu R, Weng H, Fang Z. Topological node-line semimetal in compressed black phosphorus. *Phys Rev B* **94**, 195104 (2016).
38. Zhong C, Chen Y, Xie Y, Yang SA, Cohen ML, Zhang SB. Towards three-dimensional Weyl-surface semimetals in graphene networks. *Nanoscale* **8**, 7232-7239 (2016).
39. See supplementary information.
40. Haddadi K, Bouhemadou A, Zerarga F, Bin-Omran S. First-principles investigation of the ternary scandium based inverse-perovskite carbides Sc_3AC (A= Al, Ga, In and Tl). *Solid State Sci* **14**, 1175-1185 (2012).
41. Kanchana V, Ram S. Electronic structure and mechanical properties of Sc_3AC (A= Al, Ga, In, Tl) and Sc_3BN (B= Al, In): Ab-initio study. *Intermetallics* **23**, 39-48 (2012).
42. Yang H-Y, *et al.* Extreme magnetoresistance in the topologically trivial lanthanum monopnictide LaAs. *Phys Rev B* **96**, 235128 (2017).
43. Sun S, Wang Q, Guo P-J, Liu K, Lei H. Large magnetoresistance in LaBi: origin of field-induced resistivity upturn and plateau in compensated semimetals. *New J Phys* **18**, 082002 (2016).
44. Zeng L-K, *et al.* Compensated semimetal LaSb with unsaturated magnetoresistance. *Phys Rev Lett* **117**, 127204 (2016).
45. Zhang X, Yu Z-M, Lu Y, Sheng X-L, Yang HY, Yang SA. Hybrid nodal loop metal: Unconventional magnetoresponse and material realization. *Phys Rev B* **97**, 125143 (2018).
46. Kresse G, Furthmüller J. Efficiency of ab-initio total energy calculations for metals and semiconductors using a plane-wave basis set. *Comput Mater Sci* **6**, 15-50 (1996).
47. Kresse G, Hafner J. Ab initio molecular dynamics for liquid metals. *Phys Rev B* **47**, 558 (1993).
48. Blöchl PE. Projector augmented-wave method. *Phys Rev B* **50**, 17953 (1994).
49. Perdew JP, *et al.* Atoms, molecules, solids, and surfaces: Applications of the generalized gradient approximation for exchange and correlation. *Phys Rev B* **46**, 6671 (1992).
50. Wu Q, Zhang S, Song H-F, Troyer M, Soluyanov AA. WannierTools : An open-source software package for novel topological materials. *Comput Phys Commun* **224**, 405-416 (2018).

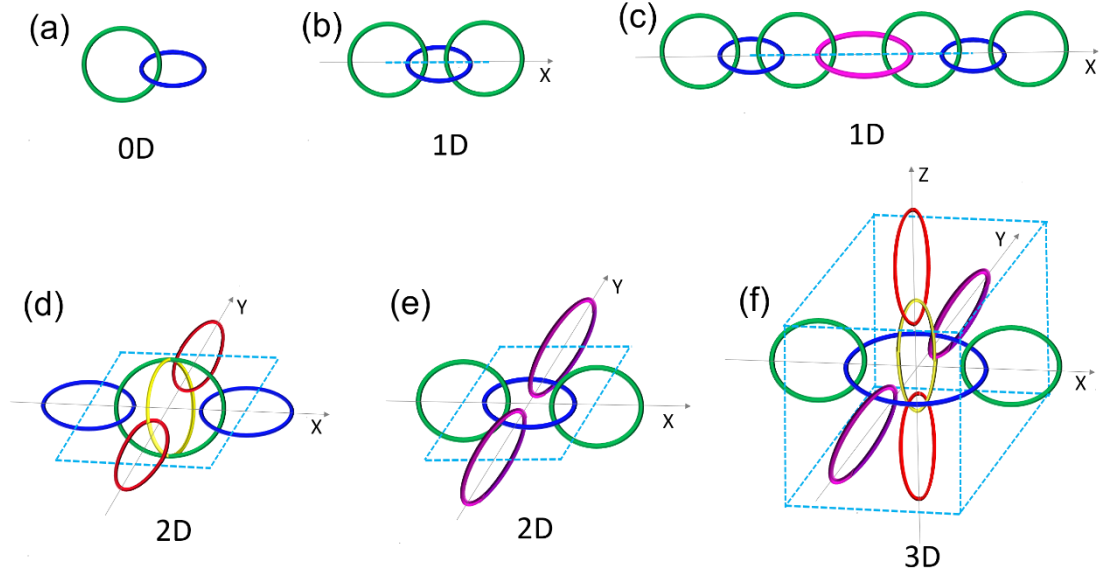


FIG.1. Hopf link, Hopf chains and Hopf-chain networks. (a) Hopf link. (b) 1D Hopf chain with a unit consisting of one Hopf link. (c) 1D Hopf chain with a unit consisting of two Hopf links. (d-e) 2D Hopf-chain networks formed by two mutually vertical chains along X and Y axes. The difference between the two networks is that the two vertical chains in (e) share a blue ring while those in (d) intersect each other. (f) 3D Hopf-chain network, consisting of a 2D network like that in (e) and a 1D chain like that in (b) along Z direction, where the 1D chain crosses over the 2D network without any contacts. The unit length of each periodic structure is labeled as light-blue dashed lines.

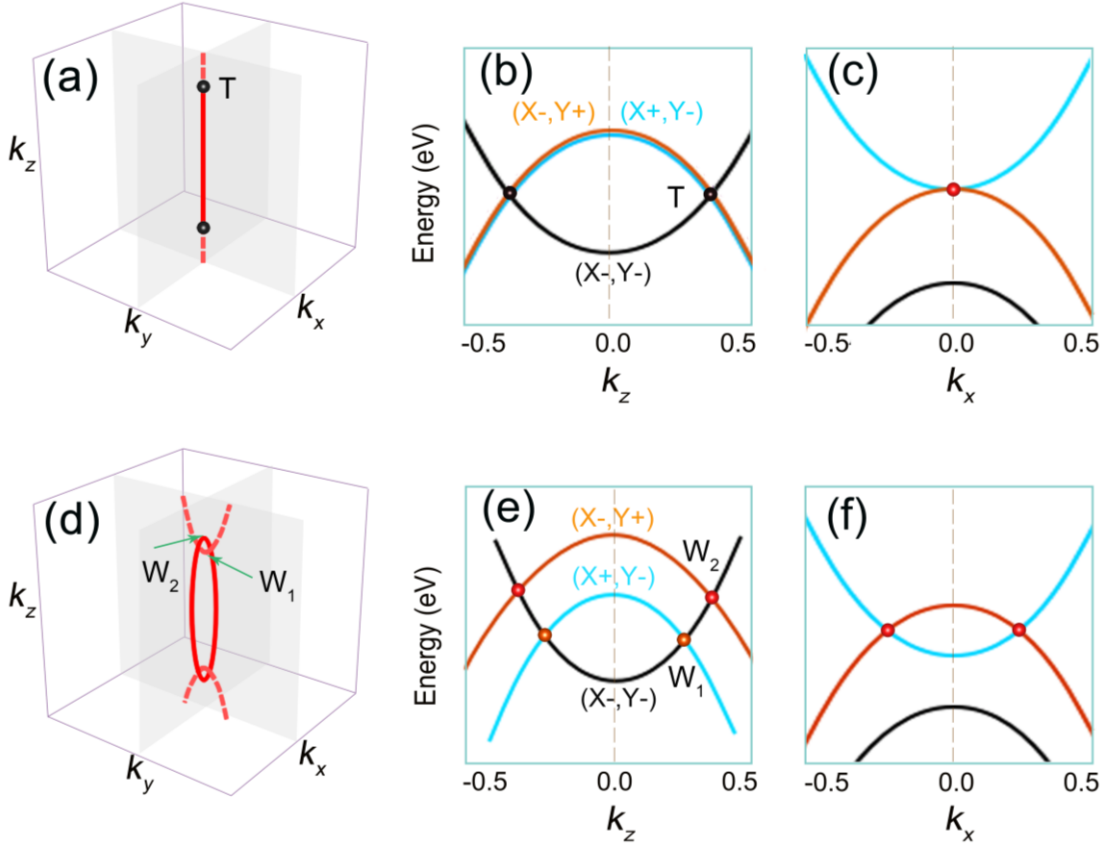


FIG.2. Transition from a triple-points phase to a 1D Hopf chain. (a) A triple-points phase, where two (black) triple points T are connected by a (red) straight nodal line along k_z axis. (b-c) Band structures corresponding to the phase in (a) along k_z and k_x axes, respectively. (d) A 1D Hopf chain where two nodal rings link each other. One ring is located on the $k_y = 0$ plane and centered at Γ point, while the other ring is located on the $k_x = 0$ plane. (e-f) Band structures corresponding to the phase in (d) along k_z and k_x axes, respectively. The phase transition from (a) to (d) is induced by the elimination of C_4 rotation symmetry. The double degenerate band in (b) splits into two bands in (e), which results in the triple point T in (b) splitting into two crossing points W_1 and W_2 in (e). X^\pm and Y^\pm in the parentheses in (b) and (e) represent the eigenvalues of mirror planes $k_x = 0$, $k_y = 0$ being ± 1 .

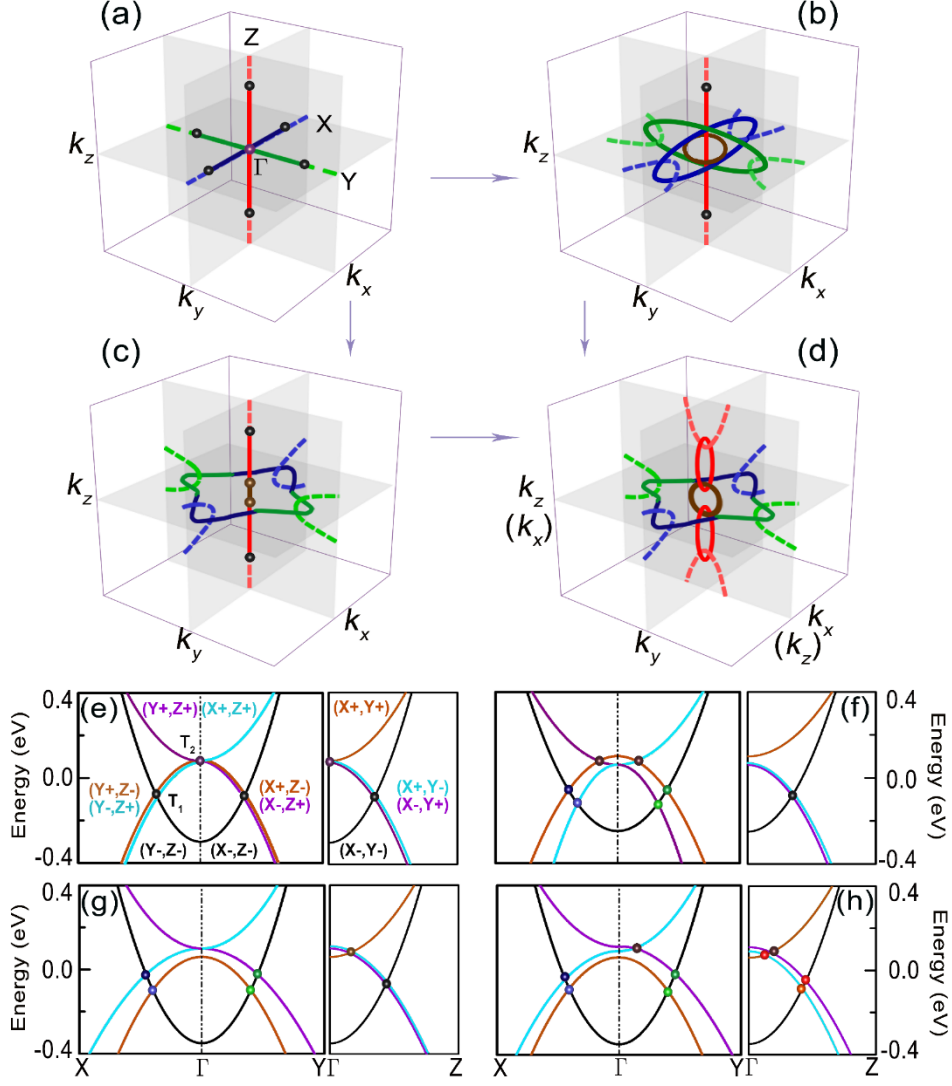


FIG.3. Transition from a 3D triple-points phase to 2D/3D Hopf-chain networks. (a) A 3D triple-points phase with 7 triple points, which is a 3D version of the phase in Fig. 2(a). (b) A mixture phase of a 2D Hopf-chain network (like that in Fig. 1(d)), a nodal ring and two triple points. (c) A mixture phase of a 2D Hopf-chain network (like that in Fig. 1(e)), and four triple points. (d) A 3D Hopf-chain networks. (e-h) Band structures corresponding to the phases in (a-d), respectively, in which $X\pm$, $Y\pm$ and $Z\pm$ in the parentheses represent the eigenvalues of mirror planes $k_x=0$, $k_y=0$ and $k_z=0$ being ± 1 . All the phases and corresponding band structures are generated by Eq. (1) with different parameters. The phase in (a) is protected by three normal C_4 rotation axes along $k_{x/y/z}$ and three mirror planes. When the C_4 rotation axes along $k_{x/y}$ are broken, it evolves into the phases in (b) and (c). When the C_4 rotation axis along k_z is further broken, the phases (b) and (c) evolve into the phase in (d). The coordinate axes in and out the parentheses in (d) represent the axes for the phase transiting from (b) and (c), respectively.

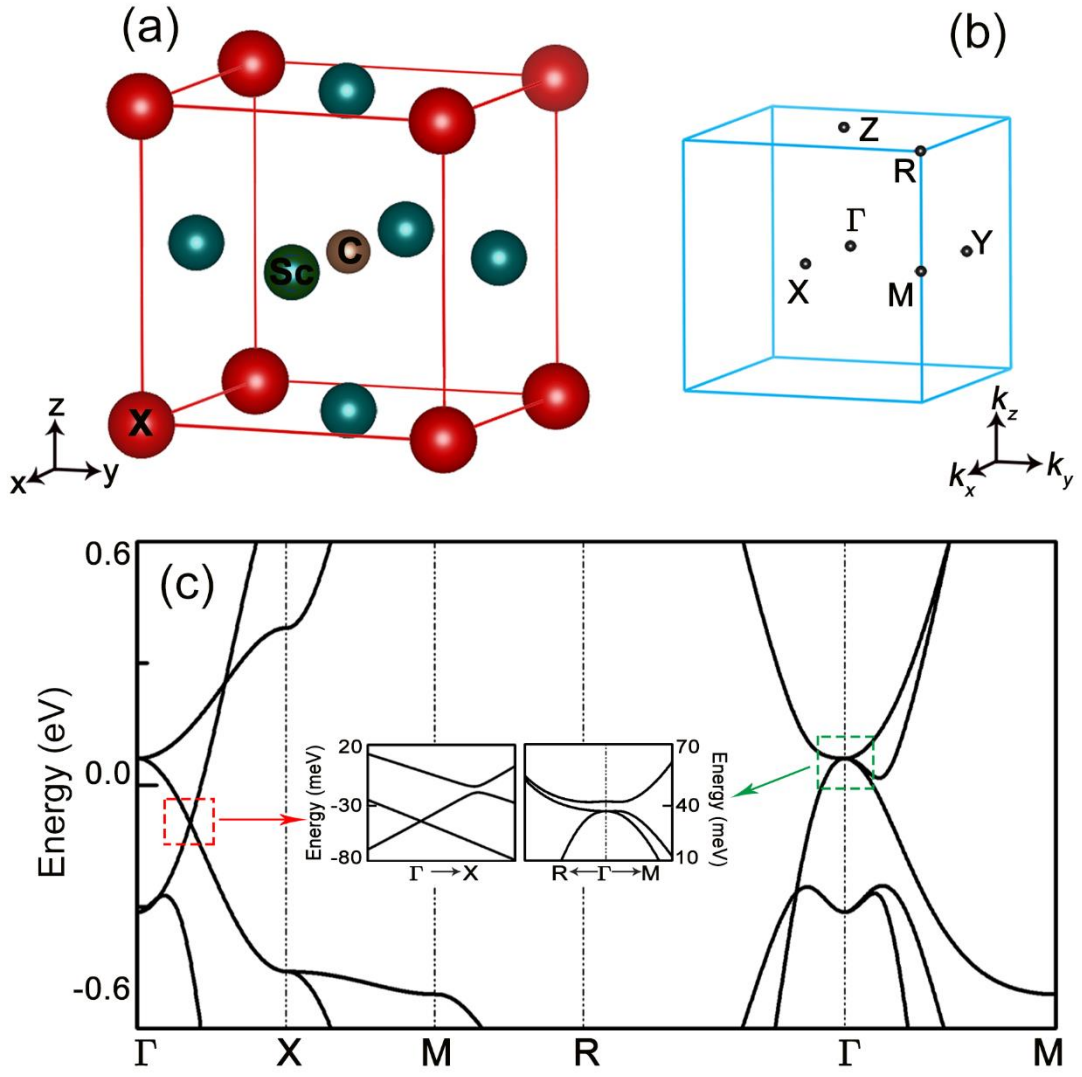


FIG. 4. **Material realizations of the triple-points and 2D/3D Hopf-chain networks in Sc_3XC .** (a) Crystal structure of Sc_3XC ($X = \text{Al, Ga, In, Tl}$). (b) BZ with high-symmetry points marked. (c) Band structure of Sc_3InC in the case of no SOC, and the insets show the band structures near the triple points in the case of considering SOC.